Research
Material Science and Engineering—Article

Biomimetic Macrophage–Fe₃O₄@PLGA Particle-Triggered Intelligent Catalysis for Killing Multidrug-Resistant *Escherichia coli*

Jieni Fu [a,b], Xiangmei Liu [c], Zhaoyang Li [a], Yufeng Zheng [b], Yu Zhang [d], Hui Jiang [a], Yanqin Liang [a], Shengli Zhu [a], Zhenduo Cui [a], Shuilin Wu [a,b,∗]

[a] *Key Laboratory of Advanced Ceramics and Machining Technology of the Ministry of Education, School of Materials Science and Engineering, Tianjin University, Tianjin 300401, China*
[b] *School of Materials Science and Engineering, Peking University, Beijing 100871, China*
[c] *School of Health Sciences and Biomedical Engineering, Hebei University of Technology, Tianjin 300401, China*
[d] *Department of Orthopedics, Guangdong Provincial People's Hospital, Guangdong Academy of Medical Sciences, Guangzhou 510080, China*

ARTICLE INFO

ABSTRACT

Infections with multidrug-resistant (MRD) Gram-negative bacteria, such as MRD *Escherichia coli* (*E. coli*), remain a challenge due to the lack of safe antibiotics and high fatality rates under anti-infection therapies. This work presents a form of biomimetic intelligent catalysis inspired by the selective biocatalytic property of macrophages, consisting of an intelligent controlling center (a living macrophage, MΦ) and a Fenton reaction catalyst (Fe₃O₄@poly(lactic-*co*-glycolic acid) (PLGA) nanoparticles) for killing MDR *E. coli* without harming normal cells. The MΦ–Fe₃O₄@PLGA particles (i.e., the intelligent catalysis particles) exhibit selective biocatalysis activity toward MDR *E. coli* by producing H₂O₂ and lipid droplets (LDs). This process activates the lipid metabolism and glycan biosynthesis and metabolism pathways based on the result of RNA sequencing data analysis. The H₂O₂ further reacts with Fe₃O₄@PLGA to form highly toxic hydroxyl radicals (•OH), while the LDs contain antimicrobial peptides and can target MDR *E. coli*. The highly toxic •OH and antimicrobial peptides are shown to combat with MDR *E. coli*, such that the antibacterial efficiency of the MΦ–Fe₃O₄@PLGA particles against MDR *E. coli* is 99.29% ± 0.31% *in vitro*. More importantly, after several passages, the intelligent catalysis function of the MΦ–Fe₃O₄@PLGA particles is well maintained. Hence, the concept of biomimetic intelligent catalysts displays potential for treating diseases other than infections.

1. Introduction

Multidrug-resistant (MDR) *Escherichia coli* (*E. coli*) infections pose a considerable threat to global public health, with devastating consequences to patient healthcare [1]. MDR Gram-negative infections pose the risk of making current antibiotic treatments ineffective due to the presence of two membranes (the inner and outer membranes) on the bacteria [2,3] and the production of β-lactamases from bacteria [4]. Unfortunately, the discovery period for new antibiotics is 6–10 years long, whereas bacteria can evolve to tolerate 1000 times greater antibiotic concentrations than their wild-type ancestors within less than 2 weeks under laboratory conditions [5,6]. More importantly, a recent study reported that

MDR *E. coli* also showed resistance to the last-resort antibiotic colistin [7–9]. Ten million people per year will be killed due to a lack of effective antibiotics by 2050 [10]. Thus, it is urgent to develop an alternative strategy for effective and safe treatment against MDR *E. coli*.

Many strategies have been used in an attempt to address this issue, such as photoexcited quantum dots [11], probiotic-based nanoparticles (NPs) [12], and microwave-responsive *Garcinia* NPs [13]. These antibacterial strategies are mainly related to the generation of heat, reactive oxygen species (ROS), or antimicrobial peptides. However, they have a long way to go before clinical application. An ideal strategy would be to use US Food and Drug Administration (FDA)-approved materials to selectively kill pathogens while leaving normal cells undamaged. As one of the critical innate immune cells, macrophages (MΦs) play a vital role in preventing microbial invasion through ROS generated by biocatalytic process [14–16]. Importantly, MΦs only clear pathogens or

apoptotic cells and do not attack normal cells, thanks to the receptors on the cell membrane. Considering their selectivity to normal cells and pathogens, MΦs have the potential for safely treating MDR *E. coli* infections. However, their physiological H_2O_2 concentrations (50–100 μmol·L^{-1}) are too low for antibacterial activity. Fortunately, MΦs can be programmed by external stimuli due to their plastic phenotype [17,18]. Pathogens and NPs (e.g., iron oxide NPs [19], CuS NPs [20], and Fe_3O_4@C/MnO_2-PGEA (PGEA is short for ethanolamine-functionalized poly(glycidyl methacrylate) [21]) can stimulate MΦs to produce H_2O_2. Among them, ferumoxytol and other iron oxide NPs have been approved by the FDA [19]. Poly (lactic-*co*-glycolic acid) (PLGA) has also been approved by the FDA [22]. Moreover, iron oxide NPs present dual enzyme-like activity both *in vitro* and *in vivo*, as they can react with H_2O_2 to form highly toxic ROS—namely, hydroxyl radicals (•OH)—in an acidic environment [23]. The bacterial infectious microenvironment has a low (i.e., acidic) pH [24]. Thus, macrophage-loaded Fe_3O_4@PLGA (MΦ–Fe_3O_4@PLGA) particles have behavior of intelligent catalysis, which could happen Fenton reaction to kill pathogen but without harming normal cells.

Here, we introduce an intelligent catalysis particle that kills MDR *E. coli* in a controlled manner without harming normal cells, by integrating an intelligent control center with a Fenton reaction catalyst. As shown in Fig. 1, this platform takes advantage of MΦ–Fe_3O_4@PLGA particles to produce H_2O_2 and lipid droplets (LDs) under the stimulation of MDR *E. coli*. These processes trigger the pathways of energy metabolism, infectious disease (bacterial), glycan biosynthesis and metabolism, and lipid metabolism. Moreover, the H_2O_2 produced further reacts with the Fe_3O_4 NPs to produce

highly toxic •OH. Furthermore, the LDs contain many antipathogenic proteins, which can target MDR *E. coli*. The antibacterial efficiency of the MΦ–Fe_3O_4@PLGA particles against MDR *E. coli* is shown to be 99.29% ± 0.31% *in vitro*. The MΦ–Fe_3O_4@PLGA particles are also activated *in vivo* and exhibit an excellent treatment effect on peritonitis *in vivo*.

2. Materials and methods

2.1. Chemicals

Iron chloride hexahydrate ($FeCl_3$), dimethyl sulfoxide (DMSO), absolute ethanol (CH_3CH_2OH), ethylene glycol (($CH_2OH)_2$), and sodium acetate (CH_3COONa) were obtained from Sinopharm Chemical Reagent Co., Ltd. (China). Sodium citrate ($C_6H_5Na_3O_7$), β-glycerol phosphate, dexamethasone, L-ascorbic acid, 3-[4,5-dime thylthiazol-2-yl]-2,5-diphenyl tetrazolium bromide (MTT), and PLGA (lactide:glycolide (50:50), molecular weight 30 000–60 000) were purchased from Sigma Chemical Co. (USA). Trypsin-EDTA, penicillin and streptomycin, fluorescein-5-isothiocyanate (FITC)-conjugated phalloidin (actin), and 4′,6-diamidino-2-phenylindole (DAPI) were obtained from Yeasen (China). Fetal bovine serum (FBS) was obtained from Gibco (US). An alkaline phosphatase (AKP) assay kit (microplate test kit) was purchased from Nanjing Jiancheng Bioengineering Institute (China). A BCA Protein Assay Kit was purchased from Solarbio (China). 2′,7′-Dichlorofluorescein diacetate (DCFH-DA) was purchased from the Beyotime Institute of Biotechnology (China). PrimeScript RT Master Mix and 2 × SYBR Premix Ex Taq II were obtained from TaKaRa (China).
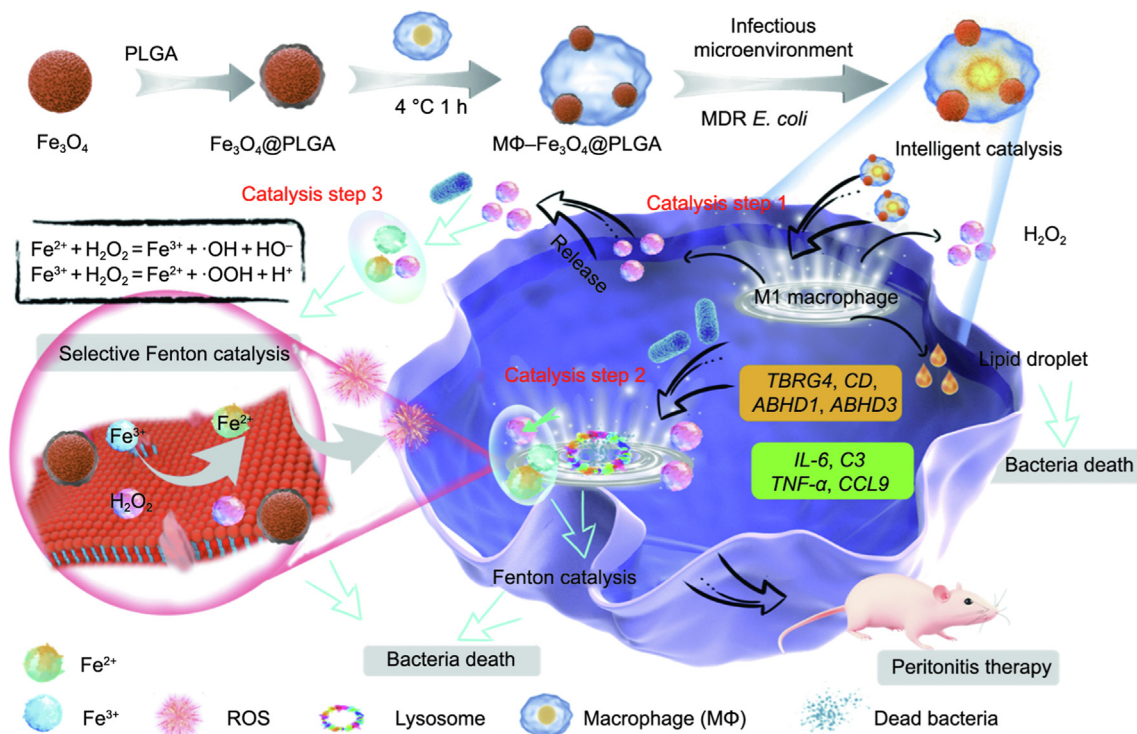
Fig. 1. Intelligent catalysis-therapeutic schematics of MΦ–Fe_3O_4@PLGA particles. Construction of MΦ–Fe_3O_4@PLGA particles from natural MΦs and Fe_3O_4@PLGA NPs. The MΦ–Fe_3O_4@PLGA particles permit controlled catalysis for killing MDR *E. coli* without harming normal cells. At catalysis step 1, the MΦ–Fe_3O_4@PLGA particles produce H_2O_2 and lipid droplets (LDs) in response to pathogens by means of the M1-like polarization of the MΦ. At catalysis step 2, the LDs contain antimicrobial peptides, which target the MDR *E. coli*. The H_2O_2 further reacts with the Fe_3O_4@PLGA NPs to trigger a Fenton reaction that produces highly toxic ROS. The LDs and ROS kill the intracellular bacteria. At catalysis step 3, the MΦ–Fe_3O_4@PLGA releases H_2O_2 outside the cells, which reacts with the Fe_3O_4@PLGA NPs to produce highly toxic ROS to kill MDR *E. coli* in the infectious microenvironment. Finally, the MΦ–Fe_3O_4@PLGA exhibits an excellent treatment effect toward peritonitis *in vivo*. *TBRG4*: transforming growth factor β regulator 4; *CD*: cluster of differentiation antigen; *ABHD1*: abhydrolase domain containing 1; *ABHD3*: abhydrolase domain containing 3; *IL-6*: interleukin 6; *C3*: complement component 3; *TNF-α*: tumor necrosis factor-α; *CCL9*: chemokine (C–C motif) ligand 9.

2.2. Cells and bacteria

Raw 264.7, L929, NIH3T3, A549, MC3T3-E1 and bone marrow mesenchymal stem cells (BMSCs, two passages) were obtained from Nankai University (China) and cultured in growth mediums. The L929, NIH3T3, A549, MC3T3-E1, and BMSCs were cultured in 89% (v/v) basic medium, 10% (v/v) FBS (OriCell), and 1% (v/v) penicillin–streptomycin (10 000 U·mL^{-1}, Gibco). For the L929 and NIH3T3 cells, the basic medium was Dulbecco's modified Eagle's medium (DMEM, Biosharp, China). For the A549 cells and BMSCs, the basic medium was DMEM/Nutrient Mixture F-12 and α-minimum essential medium (α-MEM), respectively. MC3T3-E1 also used α-MEM as basic medium. The growth medium of the Raw 264.7 cells, macrophage or MΦ, was 90% (v/v) DMEM and 10% (v/v) FBS.

MDR $E.\ coli$ (China Center of Industrial Culture Collection (CICC), 10663) was grown in Luria–Bertani (LB) broth at 37 °C. MDR $E.\ coli$ is resistant to the following antibiotics: gentamicin β-lactam antibiotics, ceftriaxone antibiotics, sulfisoxazole antibiotics, trimethoprim antibiotics, tetracycline antibiotics, and amoxicillin antibiotics.

2.3. Synthesis of Fe$_3$O$_4$ NPs

First, 1.62 g of FeCl$_3$ and 7.2 g of anhydrous sodium acetate (CH$_3$COONa) were dissolved in 100 mL of (CH$_2$OH)$_2$ and underwent magnetic stirring for 3 h. Next, the solution was sealed in Teflon-lined stainless steel at 200 °C for 8 h to obtain solid particles. After this, the black solid particles were washed with CH$_3$CH$_2$OH three times (7000 r·min^{-1}, 3 min) and dried in a vacuum for 24 h at 60 °C. These particles are referred to herein as Fe$_3$O$_4$ NPs.

2.4. Synthesis of Fe$_3$O$_4$@PLGA NPs

The synthesis of the Fe$_3$O$_4$/PLGA NPs consisted of several steps, which were as follows. First, PLGA was dissolved in DMSO to make 1% (w/v) PLGA solution. Second, the PLGA solution was mixed with Fe$_3$O$_4$ solution (0.5 mg·mL^{-1} in deionized water) at a volume ratio of 1 to 100 under ultrasonic assistance and then cleaned with CH$_3$-CH$_2$OH after centrifugation for 5 min at 7000 r·min^{-1}. The final samples are referred to herein as Fe$_3$O$_4$@PLGA NPs.

2.5. Synthesis of MΦ–Fe$_3$O$_4$@PLGA particles

To fabricate the MΦ–Fe$_3$O$_4$@PLGA particles, 2 mg of Fe$_3$O$_4$@-PLGA NPs and 1 mL of Raw 264.7 (MΦs, 1 × 10^6 cells per milliliter of DMEM) were co-cultured at 4 °C for 1 h to allow MΦs to uptake the Fe$_3$O$_4$@PLGA NPs to form MΦ–Fe$_3$O$_4$@PLGA particles. Finally, the MΦ–Fe$_3$O$_4$@PLGA particles were washed three times with DMEM.

2.6. Synthesis of FITC–Fe$_3$O$_4$@PLGA NPs

FITC–Fe$_3$O$_4$@PLGA NPs were synthesized through a modified method. First, 1 mL of FITC (0.1 μmol·L^{-1}) was dissolved in methanol, and 10 mg of Fe$_3$O$_4$@PLGA NPs was dispersed in 4 mL of methanol. Then, these solutions were thoroughly mixed via ultrasound. Next, the mixture was added to a pure 1-tetradecanol drop by drop. After stirring at 90 °C for 2 h, the methanol was evaporated. Next, the mixture was centrifuged at 10 000 r·min^{-1} for 3 min and washed with ultrapure water three times to obtain FITC–Fe$_3$O$_4$@PLGA NPs.

2.7. Characterization of Fe$_3$O$_4$@PLGA NPs

X-ray diffractometry (XRD; D8 Advanced, Bruker, Germany) using Cu Kα radiation was used to determine the crystal structure of the Fe$_3$O$_4$ NPs and Fe$_3$O$_4$/PLGA NPs. Fourier-transform infrared spectroscopy (FTIR; Nicolet IS 10, Thermo Fisher Scientific, USA) was performed to analyze the compositions of the different samples. Scanning electron microscopy (SEM; S4800, Hitachi High-Technologies Corporation, Japan) was used to characterize the morphologies of the different samples. Transmission electron microscopy (TEM; FEI-Tecnai G2 Spirit TWIN and FEI-Talos F200X, FEI company, USA) was used to obtain images of the samples.

2.8. ROS detection

2.8.1. Production of ROS by cells

Culture media from different groups (MΦs alone, co-cultured MΦs with MDR $E.\ coli$, MΦ–Fe$_3$O$_4$@PLGA particles, and co-cultured MΦ–Fe$_3$O$_4$@PLGA particles with MDR $E.\ coli$) was collected for the detection of ROS. Hydroxyl radicals were characterized by means of 3′-(p-hydroxyphenyl) fluorescein (HPF; 10 mmol·L^{-1}) at 37 °C for 30 min. Finally, the optical density was obtained using an emission wavelength of 515 nm (excitation wavelength: 490 nm). H$_2$O$_2$ was measured using a catalase (CAT) assay kit (visible light, Nanjing JiancCheng Bioengineering Institute, China).

2.8.2. Intracellular ROS detection

The cell-permeable fluorogenic probe DCFH-DA (10 μmol·L^{-1}) was used to determine the content of intracellular ROS. Cellular esterases deacetylated the DCFH-DA into non-fluorescent DCFH after the DCFH-DA diffused into the cells. Then, the DCFH was oxidized to fluorescent 2′,7′-dichlorofluorescein in the presence of ROS. First, bacterial solution (10^6 colony forming units (CFU)·mL^{-1}) was added to the MΦ–Fe$_3$O$_4$@PLGA group and cultured at 37 °C for 4 h. Next, the DCFH-DA was added to different samples (MΦ, MΦ–Fe$_3$O$_4$@PLGA particles, and MΦ–Fe$_3$O$_4$@PLGA particles with $E.\ coli$) and cultured for 30 min at 37 °C. Finally, an inverted fluorescence microscope (IFM; Olympus, IX73, Olympus Corporation, Japan) was used to obtain the images.

2.9. Mitochondrial membrane potential and adenosine 5′-triphosphate (ATP) assay

A mitochondrial membrane potential assay kit (JC-1; SBJbio Life Sciences, China) was used to determine the mitochondrial membrane potential of the MΦs. ATP activity data was acquired using an ATP Assay Kit (Beyotime).

2.10. In vitro antibacterial assay

Bacterial cells were diluted to 2 × 10^6 mL^{-1} in each well with DMEM (pH = 6.0). After culturing with different samples for 4 h, the 20 μL liquid was spread on agar plates. Next, a glass spreader was used to spread the diluted liquid on the agar surface. Finally, the number of CFU was counted as CFU·mL^{-1}.

To determine the antibacterial concentration of the Fe$_3$O$_4$@-PLGA NPs, different concentrations of Fe$_3$O$_4$@PLGA NPs (1, 2, 4, and 8 mg·mL^{-1}) were cultured with 2 × 10^6 CFU·mL^{-1} for 4 h, respectively. Finally, the number of bacteria was assessed via spread plate.

2.11. In vitro biological performance evaluation

For transwell assays, dual-chamber transwell systems with 70 μm-sized microporous membranes were used to co-culture MC3T3-E1 cells and different groups (control, Fe_3O_4/PLGA NPs, MΦ, and MΦ–Fe_3O_4@PLGA). After co-culturing for 16 h, an MTT assay was performed on these cells; detailed steps were provided in our previous work [25].

To determine the toxicity of LDs to various normal cells (Raw 264.7, L929, NIH3T3, A549, and BMSCs), lipopolysaccharides (LPS; 500 ng·mL^{-1}) were used to treat these cells. After co-culturing for 16 h, an MTT assay was performed on these cells; detailed steps were provided in our previous work [25].

To assess the influence of the concentration of Fe_3O_4@PLGA NPs on cell viability, different concentrations of Fe_3O_4@PLGA NPs (1, 2, 4, 8, 16, and 32 mg·mL^{-1}) were respectively cultured with 10^4 cells per well for 24 h. Finally, the cell viability was analyzed via MTT assay.

2.12. In vitro cellular fluorescence assay

For cell live/dead staining, 200 mL of solution (2 mg·mL^{-1} Fe_3O_4 NPs or 2 mg·mL^{-1} Fe_3O_4/PLGA NPs mixed with 10^6 mL^{-1}, respectively) was co-cultured at 4 °C for 1 h. Next, the medium was removed, and 200 mL of phosphate-buffered saline (PBS) containing fluorescent dyes (1 μmol·L^{-1} calcein AM (Ca-AM) and 10 μg·mL^{-1} propidium iodide (PI)) was added. Next, the MΦs were washed three times with PBS after incubating for 30 min. Finally, images were obtained with an IFM.

To determine the distribution of the Fe_3O_4/PLGA NPs in MΦ–Fe_3O_4@PLGA, Raw 264.7 (10^6 cells) was collected by centrifuging at 2000 r·min^{-1} for 3 min. The obtained Raw 264.7 was then co-cultured with 2 mg of FITC–Fe_3O_4@PLGA NPs at 4 °C for 1 h. Next, the mixture was centrifuged at 2000 r·min^{-1} for 3 min and then washed with DMEM three times. Then, the MΦ–FITC–Fe_3O_4@PLGA was fixed in 4% formaldehyde solution. After washing with PBS solution three times, the actin was stained with tetramethylrhodamine (TRITC)-conjugated phalloidin. Finally, images were obtained via laser scanning confocal microscopy (Nikon A1R+, Nikon, Japan).

For lysosome staining, Raw 264.7 (10^6 cells) was collected by centrifuging at 2000 r·min^{-1} for 3 min. The Raw 264.7 was then co-cultured with 2 mg of FITC–Fe_3O_4@PLGA NPs at 4 °C for 1 h. Next, the lysosome was cultured with LysoTracker Red for 20 min. Then, the medium was removed and fresh growth medium was added. Finally, images were obtained via laser scanning confocal microscopy.

2.13. RNA-sequence analysis

TRIzol reagent (Invitrogen, Thermo Fisher Scientific Inc., USA) was used to extract the total RNA. Nanodrop 2000 and agarose gel electrophoresis were performed to determine the concentration and purity of the RNA and to assess RNA integrity. The data were analyzed on the Majorbio Cloud Platform.

2.14. Multiple kinds of analyses

RSEM (version 1.3.1) was used to assess the relationship between these samples. The false discovery rate method was corrected for *P* value. DESeq2, DEGseq, and edgeR were used to obtain a gene differential expression analysis, which was further applied to gene ontology (GO) and the Kyoto Encyclopedia of Genes and Genomes (KEGG) pathway. The GO and KEGG pathway analyses were processed using Fisher's exact test and the χ^2 test.

2.15. In vivo antibacterial assay

BALb/c mice were used for *in vivo* antibacterial experiments with a peritonitis model. Animal testing was performed following the Guide for the Care and Use of Laboratory Animals of the National Institutes of Health. The Animal Ethical and Welfare Committee (AEWC) of the Institute of Radiation Medicine, Chinese Academy of Medical Sciences, approved the ethical part of the experiment. A total of 48 male BALb/c mice weighing about 20 g were divided into four groups. The DMEM, MΦ, Fe_3O_4@PLGA, and MΦ–Fe_3O_4@PLGA groups were respectively injected with 100 μL of DMEM solution containing 10^8 CFU of *E. coli*, 100 μL of DMEM solution containing 2×10^6 MΦ cells and 10^8 CFU *E. coli*, 100 μL of DMEM solution containing 2 mg of Fe_3O_4@PLGA NPs and 10^8 CFU *E. coli*, or 100 μL of DMEM solution containing 100 μL of MΦ–Fe_3O_4@PLGA particles (2×10^6 cells–2 mg Fe_3O_4@PLGA NPs) containing 10^8 CFU *E. coli*. Finally, a histopathological evaluation and blood routine assay were performed at the appropriate time.

2.16. Flow cytometry in vivo

The peritoneal lavage was collected with cold PBS solution. Seventy-micrometer nylon strainers were used to prepare single-cell suspensions. Then, Fc receptor binding inhibitor diluted 1:10 in PBS containing Zombie-Aqua fixable viability stain was used to exclude dead cells by co-culturing with the cells for 15 min on ice. The cells were then incubated according to the manufacturers' instructions using dilutions of fluorescently labeled primary monoclonal antibodies. The following antibodies were used: PerCP/Cyanine5.5 anti-mouse CD11c and PE anti-mouse CD206 antibody. Data were obtained by means of an Agilent flow cytometer (NovoCyte 2000, ACEA Biosciences, Inc., USA).

2.17. Statistical analysis

Data are presented as mean ± standard deviation (SD). Paired or unpaired *t*-tests, one-way analysis of variance (ANOVA), and two-way ANOVA were used in the statistical analyses. $P < 0.05$ was considered statistically significant.

3. Results and discussion

3.1. Characteristics of MΦ–Fe_3O_4@PLGA particles and their intelligent identification of bacteria and cells

The design of the MΦ–Fe_3O_4@PLGA particles relied on the phagocytosis of the MΦs of the Fe_3O_4@PLGA NPs. The fabrication process is illustrated in Fig. 2(a). First, 0.01% (w/v) PLGA solution was used to modify the Fe_3O_4 NPs to form Fe_3O_4@PLGA NPs. Next, the MΦs were collected using trypsin and co-cultured with the Fe_3O_4@PLGA NPs for 1 h at 4 °C in DMEM. Subsequently, DMEM was used to wash the above particles three times to eliminate unbound cells. Thus, the MΦ–Fe_3O_4@PLGA particles were formed. SEM was used to characterize the morphology of the Fe_3O_4 NPs and Fe_3O_4@PLGA NPs (Figs. S1 and S2 in Appendix A). The Fe_3O_4 NPs, which had a sphere-like morphology, were nearly (318.00 ± 100.66) nm in diameter (Fig. S1). As for the Fe_3O_4@PLGA NPs, the PLGA did not change the morphology of the Fe_3O_4 NPs (Fig. S2, left). Elemental mapping images showed that the carbon element was evenly distributed on the Fe_3O_4 NPs, further demonstrating that the PLGA was coated onto the Fe_3O_4 NPs (Fig. S2, right). The crystal structure of Fe_3O_4 and the Fe_3O_4@PLGA NPs was also determined from the XRD pattern (Fig. 2(b)). The peaks at (220), (311), (400), (422), (511), (440), and (533) are characteristic diffraction peaks of the Fe_3O_4 NPs [16,26]. FTIR was further used to characterize the PLGA, and strong absorption peaks at 2966,
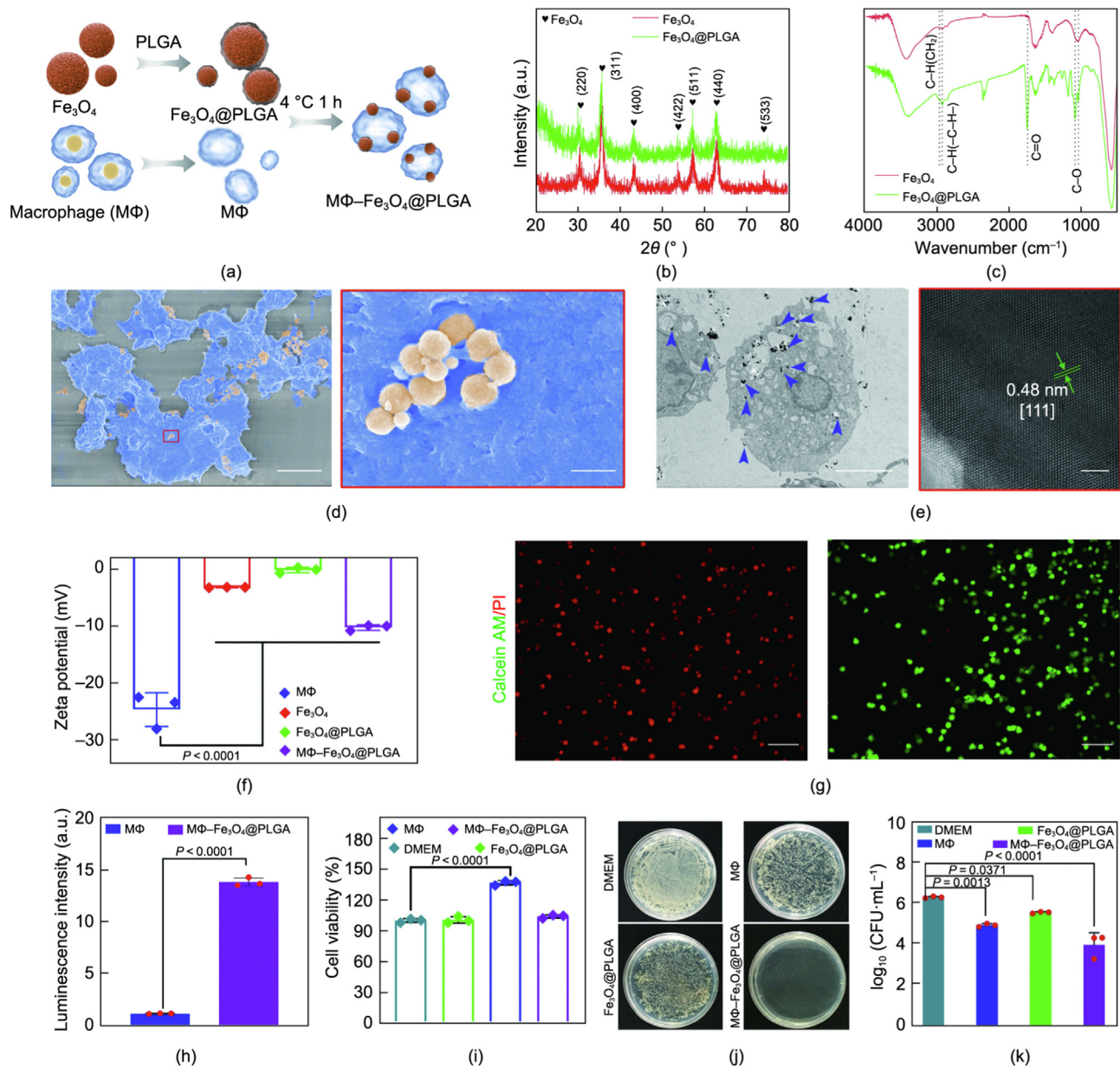
Fig. 2. Characteristics of MΦ–Fe₃O₄@PLGA particles and their intelligent identification of bacteria and cells. (a) Schematic illustration of the fabrication process of MΦ–Fe₃O₄@PLGA. (b) XRD patterns for Fe₃O₄ NPs and Fe₃O₄@PLGA NPs. (c) FTIR spectrum of Fe₃O₄ NPs and Fe₃O₄@PLGA NPs. (d) SEM images of MΦ–Fe₃O₄@PLGA particles. The MΦs and Fe₃O₄@PLGA NPs are stained blue and peach color, respectively. The scale bar of left image is 10 μm, and the scale bar of right image is 500 nm. (e) (Left) TEM image of MΦ–Fe₃O₄@PLGA particles, and the scale bar is 5 μm. (Right) HRTEM image of Fe₃O₄ NPs, and the scale bar is 5 nm. (f) Zeta potential of different samples (MΦs, Fe₃O₄ NPs, Fe₃O₄@PLGA NPs, and MΦ–Fe₃O₄@PLGA particles). (g) Live/dead staining images of (left) co-incubations of Fe₃O₄ NPs with MΦs and (right) co-incubations of Fe₃O₄@PLGA NPs with MΦs (scale bar = 100 μm); live cells are stained green with Ca-AM, and dead cells are stained red with PI. (h) ATP level of MΦs and MΦ–Fe₃O₄@PLGA particles. The experiment was carried out on $n = 3$ independent samples. (i) Cell viability of MC3T3-E1 in different groups (DMEM, Fe₃O₄@PLGA NPs, MΦs, and MΦ–Fe₃O₄@PLGA particles) for 24 h ($n = 3$ independent samples). (j) Images of the spread plate for different groups (DMEM, MΦs, Fe₃O₄@PLGA NPs, and MΦ–Fe₃O₄@PLGA particles). (k) CFU values of MDR E. coli in different groups (DMEM, MΦs, Fe₃O₄@PLGA NPs, and MΦ–Fe₃O₄@PLGA particles). The experiment was carried out on $n = 3$ independent samples. Data are expressed as mean ± SD. An ANOVA was used in parts (f, i, k), and a t-test was used in part (h).

2937, 1748, and 1078 cm⁻¹ were ascribed to the C–H stretch of CH₂, the C–H stretch of –C–H–, the stretching vibration of C=O, and the C–O stretching, respectively (Fig. 2(c)). These peaks are the characteristic peaks of the PLGA molecule [27]. The results indicated that the Fe₃O₄@PLGA NPs were successfully formed. Next, MΦ–Fe₃O₄@PLGA particles were formed, following the method illustrated in Fig. 2(a). Fig. 2(d) displayed an image of the MΦ–Fe₃O₄@PLGA particles, where the MΦs and Fe₃O₄@PLGA NPs were blue and peach in color, respectively. Fig. 2(d) (left) showed that some Fe₃O₄@PLGA NPs were bound on the surface of the MΦ. Fig. S3 (in Appendix A) also demon-

strated a similar phenomenon. Fig. 2(d) (right) further demonstrated that the morphology of the Fe₃O₄@PLGA NPs did not change on the MΦ surface. TEM images were additionally used to assess the distribution of the Fe₃O₄@PLGA in the MΦ–Fe₃O₄@-PLGA particles; they showed that the Fe₃O₄@PLGA NPs (marked by blue arrows) were associated both extracellularly and intracellularly with the MΦs (Fig. 2(e), left). The high-resolution transmission electron microscopy (HRTEM) image (Fig. 2(e), right) showed that the adjacent lattice fringes were approximately 0.48 nm, corresponding to the [111] plane of the Fe₃O₄ NPs with a cubic inverse spinel structure [28].

The zeta potential of different samples was measured, and the zeta potentials of the MΦ, Fe_3O_4 NPs, Fe_3O_4@PLGA NPs, and MΦ–Fe_3O_4@PLGA particles were found to be –24.93, –3.37, –0.31, and –10.43 mV, respectively (Fig. 2(f)). The cell membrane is negatively charged due to the phospholipid bilayer structure. Negatively charged superparamagnetic particles have been shown to exhibit a high but nonspecific affinity for the cell membrane [29]. Some Fe_3O_4@PLGA NPs were distributed on the surface of the cell membrane, and the zeta potential was increased from –24.93 to –10.43 mV. These results showed that the Fe_3O_4@PLGA NPs were successfully connected with the MΦs.

Ca-AM (green) and PI (red) were used to stain viable and dead cells. As shown in Fig. 2(g), the color of the cells was red after co-culturing the Fe_3O_4 NPs with MΦs at 4 °C for 1 h. In contrast, the cells were green after co-culturing with the Fe_3O_4@PLGA NPs. These results indicated that PLGA had a remarkable protective effect on the MΦs during the synthesis process of the MΦ–Fe_3O_4@PLGA particles. Previously, it has been demonstrated that Fe_3O_4 NPs could increase the inflammatory response of MΦs [30]. Moreover, naked superparamagnetic iron oxide NPs were found to present obvious cytotoxicity [31,32]. PLGA has a low propensity to cause immune responses and is not toxic to cells [30,31]. The Fe_3O_4 NPs were coated with PLGA, resulting in low toxicity with little or no effect on cell function and viability [33]. It should be noted that a cold experimental setting can up-regulate the expression of pro-inflammatory genes [34] and limit the phagocytic behavior of MΦ.

Adenosine triphosphate (ATP) is generally considered to be the "energy currency" of the cell [35]. The production of ATP by the MΦs in the MΦ-Fe_3O_4@PLGA particles was obviously greater than that produced by the MΦs alone (Fig. 2(h)). When MΦs are activated into M1 MΦs, their metabolism switches from oxidative phosphorylation to aerobic glycolysis—a change that has been linked to the generation of ROS [36,37]. The enhanced aerobic glycolysis can rapidly provide ATP from glucose, enhancing the ATP activity. The results indicated that the viability and function of the MΦ-Fe_3O_4@PLGA particles was not damaged by the synthesis process, and that Fe_3O_4@PLGA had the potential to induce MΦs into the M1 phenotype.

The cytotoxicity of the MΦ–Fe_3O_4@PLGA particles on normal cells was further assessed as shown in Fig. 2(i), with MC3T3-E1 being chosen as a model cell. Compared with the cell viability of MC3T3-E1 cultured with DMEM, MC3T3-E1 cultured with the MΦ–Fe_3O_4@PLGA and Fe_3O_4@PLGA groups showed slightly higher cell viability. These results suggested that the Fe_3O_4@PLGA NPs and MΦ–Fe_3O_4@PLGA particles showed excellent biocompatibility with MC3T3-E1. To further investigate the influence of the MΦ–Fe_3O_4@PLGA particles on the viability of MDR *E. coli*, the antibacterial activity of different samples (DMEM, MΦ, Fe_3O_4@PLGA, and MΦ–Fe_3O_4@PLGA) was assessed (Fig. 2(j) and (k)). Fe_3O_4@PLGA NPs with concentration of 4 mg·mL^{-1} was found to be fatal to bacteria without detriment to the MΦ by means of MTT and antibacterial assays (Figs. S4 and S5 in Appendix A). Compared with the CFU of MDR *E. coli* treated with DMEM, the CFU of MDR *E. coli* in MΦ, Fe_3O_4@PLGA, and MΦ–Fe_3O_4@PLGA were 1.37-log, 0.75-log, and 2.33-log decreases, respectively. The antibacterial efficiency against MDR *E. coli* of MΦ, Fe_3O_4@PLGA, and MΦ–Fe_3O_4@PLGA was found to be 95.74% ± 0.44%, 82.22% ± 0.95%, and 99.29% ± 0.31%, respectively (Fig. 2(j) and (k)). These results demonstrated that the MΦ–Fe_3O_4@PLGA particles could selectively kill MDR *E. coli* without harming normal cells.

3.2. In vitro characterization of the intelligent catalytic performance of MΦ–Fe_3O_4@PLGA particles

As mentioned in the earlier section on the intelligent-killing behavior of the MΦ–Fe_3O_4@PLGA particles, the MΦ–Fe_3O_4@PLGA particles were chosen for an *in vitro* study. Next, we further analyzed the influence of MDR *E. coli* on the MΦ's fate in MΦ–Fe_3O_4@PLGA or MΦ. The polarization phenotypes of the MΦs in the MΦ–Fe_3O_4@PLGA particles were characterized by means of enzyme-linked immunosorbent assay (ELISA) (Fig. 3(a)). Tumor necrosis factor-α (TNF-α) and interleukin (IL)-10 were chosen as a classical M1 marker [38] and M2 marker [39], respectively. As shown in Fig. 3(a), compared with the MΦs alone, the MΦs of the MΦ–Fe_3O_4@PLGA particles showed similar expression of the cytokines of IL-10 and TNF-α, suggesting that the Fe_3O_4@PLGA NPs did not cause MΦ polarization. In the MΦs treated with *E. coli*, the production of TNF-α was increased, but there was no significant production of IL-10, indicating that *E. coli* was able to promote the MΦs into the M1 phenotype. Unexpectedly, the concentration of TNF-α was even higher after co-culturing *E. coli* with the MΦ–Fe_3O_4@PLGA particles. This result indicated that *E. coli* promoted M1 MΦ polarization. Fluorescence-activated cell sorting (FACS) was further performed to analyze the influence of MDR *E. coli* on the polarization phenotypes of MΦ–Fe_3O_4@PLGA Figs. 3(b) and (c). Compared with the untreated MΦs, 2.63% and 3.55% of the MΦs of the MΦ–Fe_3O_4@PLGA and of the MΦ–Fe_3O_4@PLGA with *E. coli* responded to the M1 marker (CD11c), respectively, and 1.31% and 0.60% responded to the M2 marker (CD206) [38]. The ratio between M1 and M2 in the MΦ–Fe_3O_4@PLGA and MΦ–Fe_3O_4@PLGA with *E. coli* groups was 2.01 and 5.92, respectively, indicating that *E. coli* further induced M1 MΦ polarization in the MΦ–Fe_3O_4@PLGA particles. These results demonstrated that the MΦ–Fe_3O_4@PLGA was able to polarize into an M1 MΦ after treatment with MDR *E. coli*.

It is generally known that M1 MΦs release H_2O_2 [40]. H_2O_2 is an essential component of the Fenton reaction, which generates highly toxic hydroxyl radicals in the presence of iron [19]. To further assess the possibility of the Fenton reaction occurring, H_2O_2 was externally supplied to assess whether the Fe_3O_4@PLGA NPs could react with H_2O_2 to produce hydroxyl radicals. A HPF detection kit was used to detect hydroxyl radicals. As shown in Fig. 3(d), the produced hydroxyl radicals were positively related to the content of the supplied H_2O_2 (0, 2, 8, 32, 128 mmol·L^{-1}). Thus, the Fe_3O_4@PLGA NPs reacted with the H_2O_2 supplied to produce hydroxyl radicals. Moreover, co-cultures of MDR *E. coli* and MΦ–Fe_3O_4@PLGA produced 138.39 mmol·L^{-1} H_2O_2 compared with MΦs alone (51.74 mmol·L^{-1} H_2O_2; $P < 0.0001$) (Fig. 3(e)), which was a 4.80-fold increase in hydroxyl radicals compared with the MΦs ($P < 0.0001$) (Fig. 3(f)).

Next, we investigated whether co-cultures of MDR *E. coli* could enhance the intracellular accumulation of soluble iron species. The intracellular accumulation of soluble iron species of different samples was detected by means of inductively coupled plasma (ICP), as shown in Fig. 3(g). Compared with the MΦ group, the level of intracellular soluble iron was dramatically higher in the cells from Fe_3O_4@PLGA particles. This was mainly due to the presence of the Fe_3O_4@PLGA NPs. Moreover, adding MDR *E. coli* further enhanced the concentration of iron. This phenomenon indicated that the MΦ–Fe_3O_4@PLGA particles produced soluble iron species in response to MDR *E. coli*. TEM images were used to display the presence of LDs in different samples (MΦ, MΦ–Fe_3O_4@PLGA, and MΦ–Fe_3O_4@PLGA with *E. coli*) (Fig. S6 in Appendix A; Figs. 3(h) and (i)). Compared with the MΦs, there was no presence of LDs in the MΦ–Fe_3O_4@PLGA particles. After co-culturing with MDR *E. coli*, some LDs (red arrows) and MDR *E. coli* (green arrows) were present in the cells. Some LDs were located around the MDR *E. coli* (green arrows), demonstrating that the LDs could target MDR *E. coli*. LDs are major lipid storage organelles of eukaryotic cells; they contain antibacterial proteins that participate in antibacterial processes [41]. It is generally known that LDs have protein-mediated antimicrobial capacity, and infection can increase the generation of LDs.
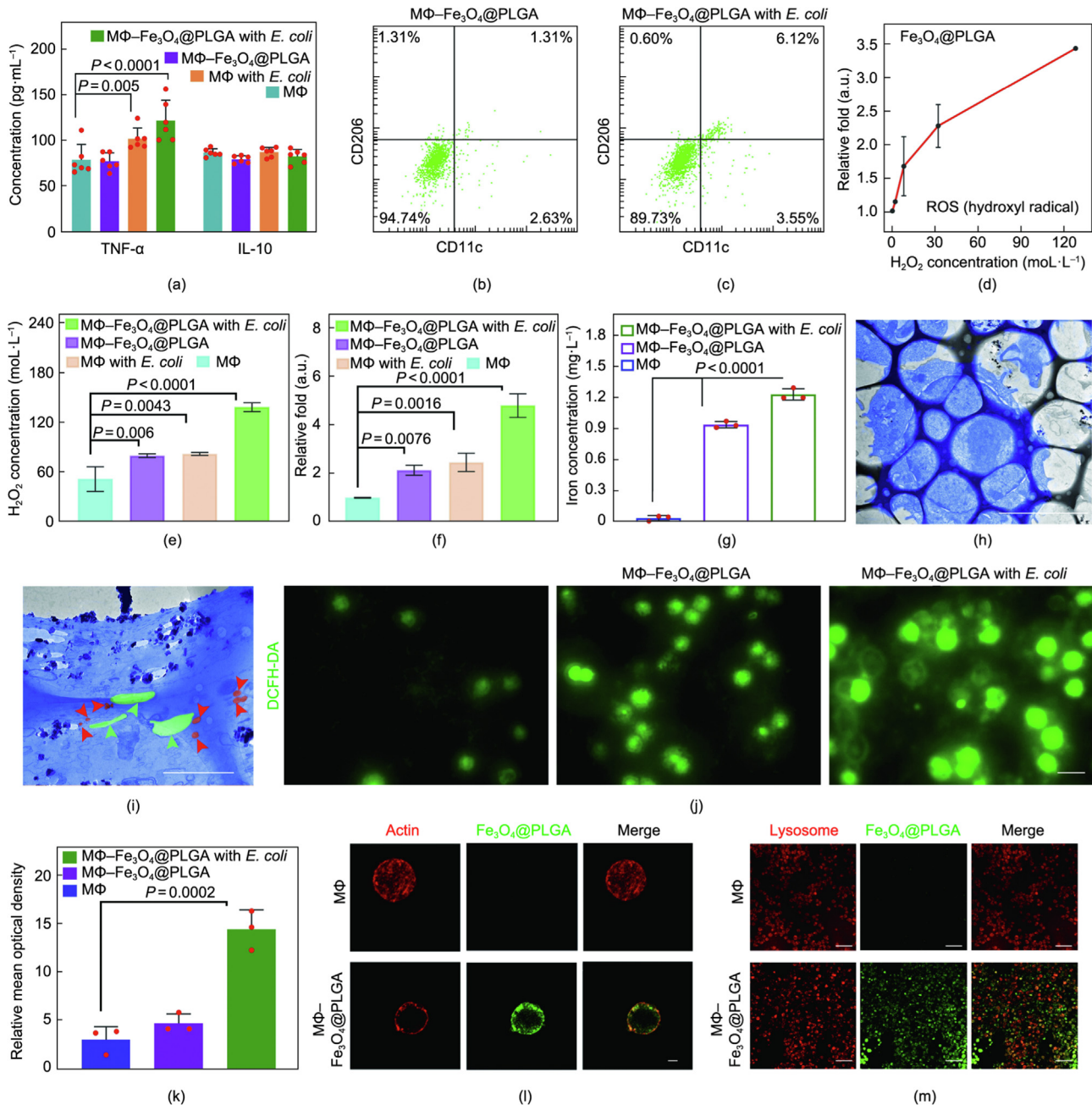
Fig. 3. *In vitro* characterization of the intelligent catalytic performance of MΦ–Fe₃O₄@PLGA particles. (a) Concentration of *TNF-α* and *IL-10* after different treatments (*n* = 6 independent samples). (b, c) FACS analysis of (b) MΦ–Fe₃O₄@PLGA particles and (c) MΦ–Fe₃O₄@PLGA with *E. coli*. (d) The relative fold number of hydroxyl radicals upon the addition of various concentrations of H_2O_2 (0, 2, 8, 32, and 128 mmol·L⁻¹). (e, f) Pro-inflammatory M1 MΦs release hydrogen peroxide, which reacts with iron to generate highly toxic hydroxyl radicals; the graph shows quantitative measures of (e) hydrogen peroxide and (f) hydroxyl radicals. (g) Intracellular ion concentration of different groups (MΦs, MΦ–Fe₃O₄@PLGA particles, and MΦ–Fe₃O₄@PLGA with *E. coli*; *n* = 3). (h, i) TEM images of (h) MΦ–Fe₃O₄@PLGA particles (scale bar = 5 μm) and (i) MΦ–Fe₃O₄@PLGA with *E. coli* (scale bar = 1 μm). LDs are indicated with red arrows and MDR *E. coli* with green arrows. (j) Intracellular ROS level of MΦ following different treatments. Cellular ROS were stained with a DCFH-DA probe (scale bar = 20 μm). (k) Corresponding quantitative fluorescence intensity of different groups (MΦ, MΦ–Fe₃O₄@PLGA, and MΦ–Fe₃O₄@PLGA with *E. coli*; *n* = 3). (l) Cellular uptake of NPs. Actin was stained with TRITC-conjugated phalloidin, and Fe₃O₄@PLGA NPs were marked by FITC (green color). The scale bar is 4 μm. (m) Lysosome escape study. Lysosomes were marked with LysoTracker Red (red color), and Fe₃O₄@PLGA NPs were labeled by FITC (green color). The scale bar is 50 μm. Data are expressed as mean ± SD; a one-way ANOVA was used in parts (e, f, j, k), and a two-way ANOVA was used in part (a).

This result indicated that LDs were formed in the MΦ–Fe₃O₄@PLGA particles after treatment with MDR *E. coli*. It is generally known that LPS can induce LD formation in cells [41]. LPS were used to treat the Raw 264.7, L929, A549, NIH3T3, and BMSCs for 16 h. As shown in Fig. S7 (in Appendix A), LPS had no toxic effect on these cells. The results suggested that LDs would not kill normal cells.

The content of intracellular ROS was detected by means of DCFH-DA [42,43]. The green fluorescence intensity of the MΦ–Fe₃-

O₄@PLGA particles was higher than that of the MΦs, suggesting that the content of intracellular ROS was enhanced in response to the Fe₃O₄@PLGA NPs. After MDR *E. coli* was added, the green fluorescence intensity was further enhanced, suggesting that MDR *E. coli* promoted the content of intracellular ROS (Fig. 3(j)). The corresponding quantitative analysis showed a similar tendency (Fig. 3 (k)). These results further confirmed that the MΦ–Fe₃O₄@PLGA particles produced more ROS in response to MDR *E. coli*. Live cell

imaging was further used to characterize the location of the ROS. The cell membrane, lysosome, intracellular ROS, and nucleus were stained with DiR, LysoTracker Red, a DCFH-DA probe, and Hoechst 33342, respectively. As shown in Fig. S8 in Appendix A, green fluorescence appeared to overlap with the red fluorescence and also existed in other areas, suggesting that ROS were produced in parts of the cell other than lysosomes. Fig. S9 (in Appendix A) further indicates that ROS were not only produced in the cells but also in the environment. FITC was used to mark the Fe$_3$O$_4$@PLGA NPs, and TRITC-labeled phalloidin was used to stain the actin of the MΦs. As shown in Fig. 3(l), the Fe$_3$O$_4$@PLGA NPs were distributed both on the membrane and in the intracellular system of the MΦs. Lysosome staining was further performed to assess whether Fe$_3$O$_4$@PLGA could enter lysosomes. As shown in Fig. 3(m), some Fe$_3$O$_4$@PLGA NPs were distributed in lysosomes. This result indicated that some of the Fe$_3$O$_4$@PLGA NPs were engulfed by lysosomes. PLGA is negatively charged, and the negatively charged NPs prefer to colocalize with endosomes and lysosomes [44]. These results demonstrated that the MΦ–Fe$_3$O$_4$@PLGA particles had intelligent catalytic ability and could activate a selective Fenton reaction in response to MDR E. coli in lysosomes and the infectious microenvironment.

3.3. Mechanism of the intelligent biocatalysis behavior of MΦ–Fe$_3$O$_4$@PLGA particles

To further analyze the underlying mechanism of the intelligent catalysis behavior of the MΦ–Fe$_3$O$_4$@PLGA particles, high-throughput sequencing was used to analyze gene expression profiles [25]. RNA-sequence analysis was performed to study the expression difference of the MΦs under different conditions (MΦs alone, MΦ with E. coli, and MΦ–Fe$_3$O$_4$@PLGA with E. coli). A total of 2030 genes were detected: 631 genes in MΦ–Fe$_3$O$_4$@PLGA with E. coli versus MΦs, 441 genes in MΦ–Fe$_3$O$_4$@PLGA with E. coli versus MΦs with E. coli, and 52 genes in MΦs with E. coli versus MΦs (Fig. 4(a)). Principal component analysis (PCA) revealed distances between different samples (MΦs, MΦs with E. coli, and MΦ–Fe$_3$O$_4$@PLGA with E. coli), suggesting that the different treatments would cause differences in gene expression (Fig. 4(b)). As shown in Figs. 4(c)–(e), the volcano plots showed 273 up-regulated genes and 43 down-regulated genes for MΦs with E. coli versus MΦs; 644 up-regulated genes and 718 down-regulated genes for MΦ–Fe$_3$O$_4$@PLGA with E. coli versus MΦs; and 408 up-regulated genes and 900 down-regulated genes for MΦ–Fe$_3$O$_4$@PLGA with E. coli versus MΦs with E. coli. This finding suggested that the treatment caused a major difference in gene expression.

A GO database analysis was performed to analyze the expression of different genes. The enriched terms of MΦ–Fe$_3$O$_4$@PLGA with E. coli versus MΦs with E. coli, and those of MΦs with E. coli versus MΦs, are shown in Fig. 4(f). The genes were rich in catalytic activity, response to stimulus, biological adhesion, and immune system process on MΦs with E. coli versus MΦs. The genes were rich in catalytic activity, antioxidant activity, response to stimulus, biological adhesion, and immune system process on MΦ–Fe$_3$O$_4$@PLGA with E. coli versus MΦs with E. coli. According to the KEGG pathway analysis, it was found that infectious disease (bacterial), immune system, lipid metabolism, and glycan biosynthesis and metabolism were up-regulated in MΦs with E. coli compared with MΦs (Fig. S10 in Appendix A). Infectious disease (bacterial), lipid metabolism, glycan biosynthesis and metabolism, and energy metabolism were up-regulated in MΦ–Fe$_3$O$_4$@PLGA with E. coli compared with MΦs with E. coli (Fig. S11 in Appendix A). These activated signaling pathways and functions resulted in M1 MΦ development and LD formation.

From the heatmap of MΦ–Fe$_3$O$_4$@PLGA with E. coli, MΦs with E. coli, and MΦs, the expression of the genes chemokine (C–C motif) ligand 9 (CCL9) [45], interleukin 6 (IL-6) [46], complement component 3 (C3) [47], schlafen 4 (SLFN4) [48], abhydrolase domain containing 3 (ABHD3) [49], abhydrolase domain containing 1 (ABHD1) [50], cluster of differentiation antigen (CD), and transforming growth factor β regulator 4 (TBRG4) [51] were changed (Fig. 4(g)). The genes of IL-6, CCL9, SLFN4, and C3 were related to the polarization of MΦs. Moreover, the genes of ABHD1, ABHD3, and CD were related to the formation of LDs in MΦs.

Mitochondria play a vital role in immunity response, and the interaction between LDs and mitochondria is decreased in infected cells [41]. The mitochondria membrane potential is a signal of mitochondria activity [33]. As shown in Fig. S12 (in Appendix A), the ratio of green/red fluorescence intensity in MΦs with E. coli was higher compared with the MΦ group, and that of the MΦ–Fe$_3$O$_4$@PLGA with E. coli group was lower compared with the MΦs with E. coli group, suggesting that the interaction between LDs and mitochondria was decreased, and that more LDs were involved in antibacterial activity. Based on the above results, the complete process of clearing MDR E. coli via MΦ–Fe$_3$O$_4$@PLGA is illustrated in Fig. 4(h). Iron oxide NPs are phagocytized by MΦs and are then degraded into iron ions within lysosomes [52]. When MΦ–Fe$_3$O$_4$@PLGA particles are co-cultured with MDR E. coli, the expression of the genes TNF-α, IL-6, CCL9, SLFN4, and C3 is up-regulated, while the expression of the gene TBRG4 is down-regulated. These results indicate that the MΦs are polarized into the M1 phenotype. The M1 MΦs release hydrogen peroxide, which generates highly toxic hydroxyl radicals (•OH) in the presence of iron ions via the Fenton reaction [53]. Furthermore, the genes of ABHD3, ABHD1, and CD were up-regulated, indicating that LDs were formed in the MΦs in response to MDR E. coli.

3.4. Viability and antibacterial ability of MΦ–Fe$_3$O$_4$@PLGA particles after several passages in vitro and biosafety assessment of MΦ–Fe$_3$O$_4$@PLGA particles in vivo

The hydroxyl radicals and LDs finally caused the death of the MDR E. coli. The viability and function of the MΦ–Fe$_3$O$_4$@PLGA particles were further evaluated by means of Ca-AM/PI staining and an antibacterial assay (Figs. 5(a) and (b)). The number of remaining cells in the MΦ–Fe$_3$O$_4$@PLGA group decreased after several passages (Fig. 5(a)). The antibacterial efficiency of MΦ–Fe$_3$O$_4$@PLGA at passages 1 and 2 was 62.04% ± 3.84% and 17.00% ± 5.44%, respectively (Fig. 5(b)). These results suggested that the function of MΦ–Fe$_3$O$_4$@PLGA was partially retained after several passages.

The aforementioned in vitro investigation demonstrated that the MΦ–Fe$_3$O$_4$@PLGA particles had excellent selectivity between pathogens and normal cells. The MΦ–Fe$_3$O$_4$@PLGA particles were therefore selected for an in vivo study. Fluorescence imaging was performed to evaluate whether the MΦ–Fe$_3$O$_4$@PLGA particles could be retained and accumulate at the infected site for enough time in vivo (Figs. 5(c)–(e)). MΦ–Fe$_3$O$_4$@PLGA-Cyanine-7 (cy7) was used for this process, and images at different time points were obtained to display the process. Compared with the pre-injection group (mice without any treatment), a significantly high fluorescence signal was shown at 0, 2, and 6 h for mice treated with MΦ–Fe$_3$O$_4$@PLGA-cy7. Moreover, the fluorescence disappeared after 24 h. This result indicated that MΦ–Fe$_3$O$_4$@PLGA was able to remain at the infected site for at least 6 h.
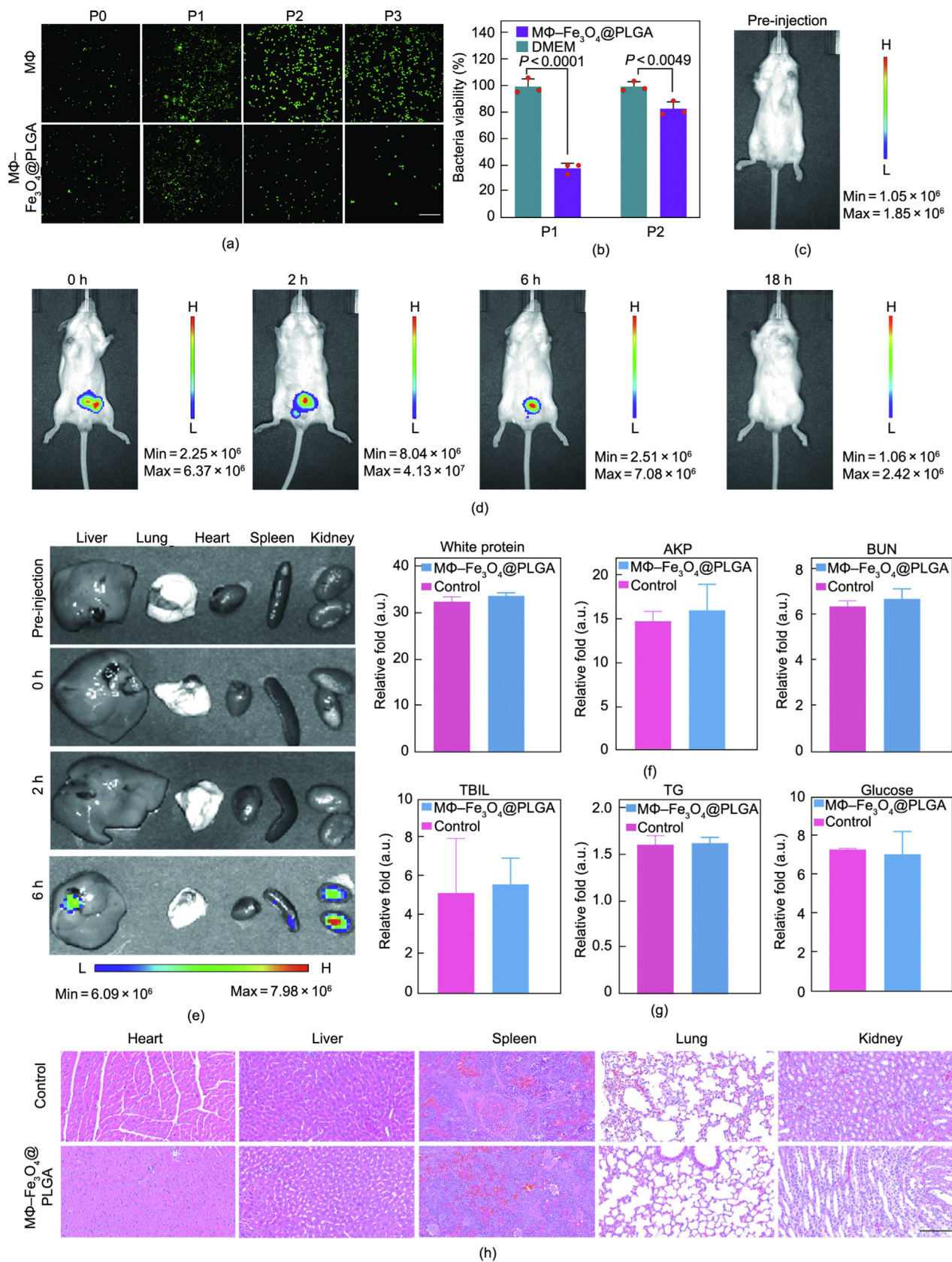
Next, fluorescence images of major organs (i.e., the liver, lung, heart, spleen, and kidney) were further used to analyze the metabolic behavior of MΦ–Fe$_3$O$_4$@PLGA. The fluorescence images of major organs showed that some MΦ–Fe$_3$O$_4$@PLGA-cy7 particles were distributed in the liver and kidney at 6 h. The imaging data demonstrated that MΦ–Fe$_3$O$_4$@PLGA could be metabolized by
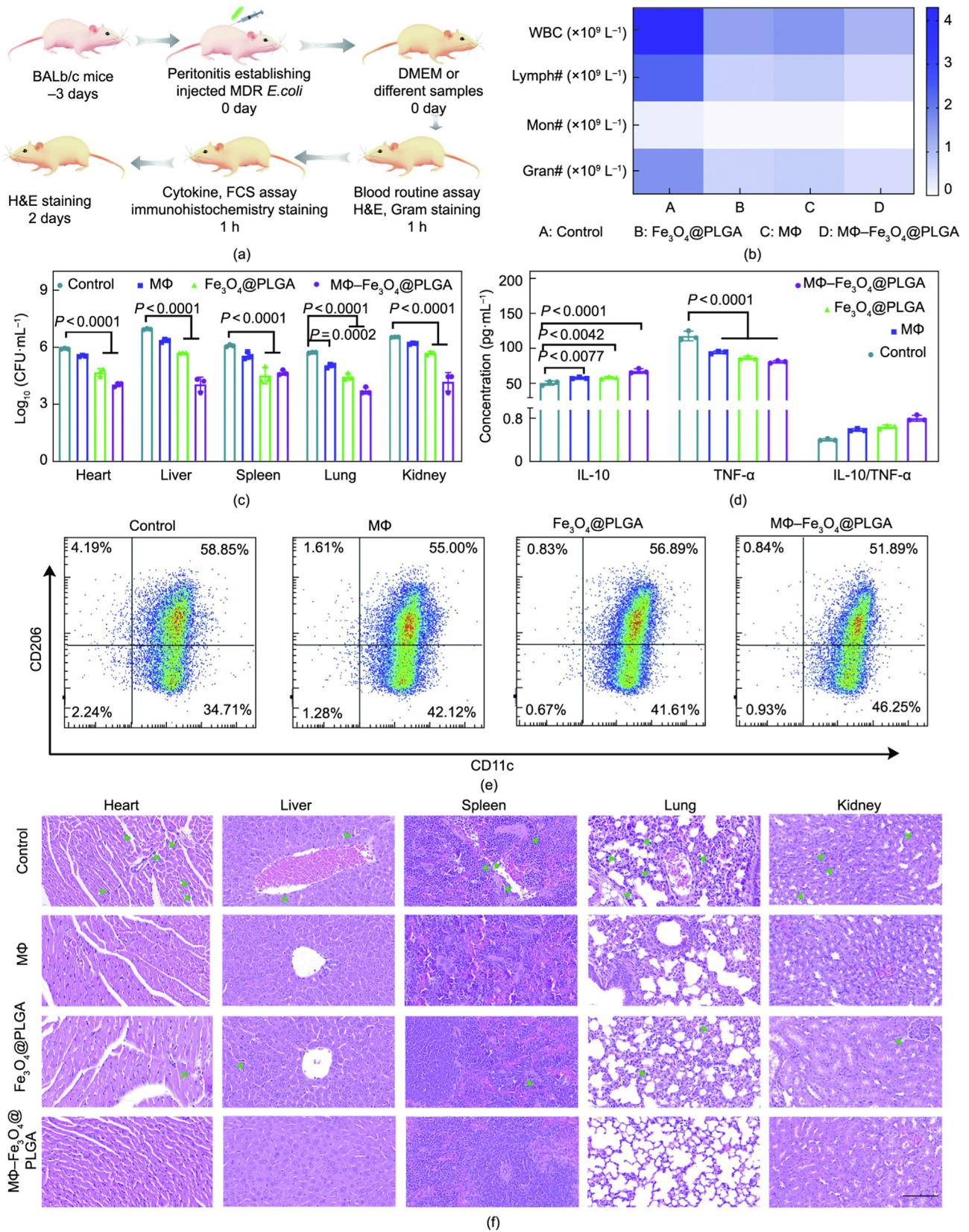
J. Fu, X. Liu, Z. Li et al.
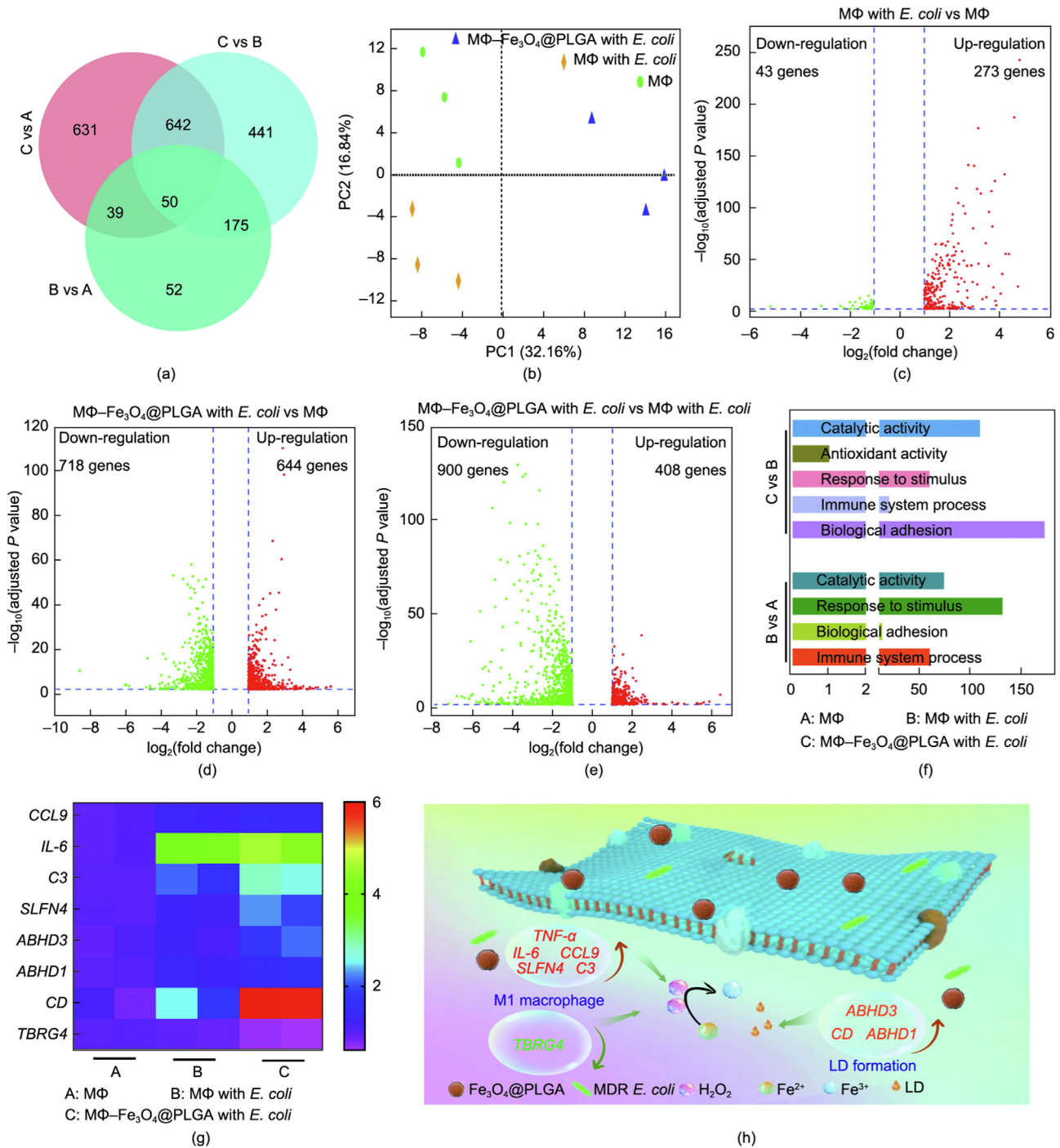
Fig. 4. Mechanism of the intelligent biocatalysis behavior of MΦ–Fe₃O₄@PLGA particles. (a) Venn diagram of differentially expressed genes in MΦs, MΦs with *E. coli*, and MΦ–Fe₃O₄@PLGA with *E. coli*. (b) PCA showing PC1 and PC2 for all RNA-sequencing data of MΦs, MΦs with *E. coli*, and MΦ–Fe₃O₄@PLGA with *E. coli*. (c–e) Volcano plot of the transcriptomic analysis of differentially expressed genes (n = 3 independent experiments per group): (c) MΦs with *E. coli* vs MΦ; (d) MΦ–Fe₃O₄@PLGA with *E. coli* vs MΦ; and (e) MΦ–Fe₃O₄@PLGA with *E. coli* vs MΦs with *E. coli*. (f) Upregulated GO enrichment analysis in MΦ–Fe₃O₄@PLGA with *E. coli* compared with MΦs, and in MΦ–Fe₃O₄@PLGA with *E. coli* compared with MΦs with *E. coli*. (g) Heat maps of cluster of genes of MΦ–Fe₃O₄@PLGA with *E. coli* and MΦs with *E. coli* in comparison with MΦs. (h) Schematic illustration of the antibacterial mechanism of MΦ–Fe₃O₄@PLGA.

Fig. 5. Viability and antibacterial ability of MΦ–Fe₃O₄@PLGA particles after several passages *in vitro* and biosafety assessment of MΦ–Fe₃O₄@PLGA particles *in vivo*. (a) Live/dead staining images of different groups (MΦs and MΦ–Fe₃O₄@PLGA NPs). Fewer MΦs are present in different passages (P1, P2, and P3) compared with the control (P0) (scale bar = 100 μm). (b) CFU values of MDR *E. coli* treated by different passages (P1 and P2) of MΦ–Fe₃O₄@PLGA NPs. The experiment was carried out on n = 3 independent samples. (c, d) *In vivo* living imaging of mice after a local injection of MΦ–Fe₃O₄@PLGA particles at different times. (e) *In vivo* living imaging of major organs after a local injection of MΦ–Fe₃O₄@PLGA particles at different times. The relative fold of (f) white protein, AKP, and BUN, (g) TBIL, TG, and glucose of each group compared with control group at the time of treatment and 1 day later. The experiment was carried out on n = 3 independent samples. (h) Representative H&E staining images of each group's heart, liver, spleen, lung, and kidney at the time of treatment and 1 day later (scale bar = 100 μm). Data are expressed as mean ± SD; a two-way ANOVA was used in part (b). H: high; L: low; BUN: blood urea nitrogen; TBIL: total bilirubin, TG: triglyceride.

J. Fu, X. Liu, Z. Li et al.

(a)

(b)

(c) Pre-injection
Min = 1.05×10^6
Max = 1.85×10^6

0 h
Min = 2.25×10^6
Max = 6.37×10^6

2 h
Min = 8.04×10^6
Max = 4.13×10^7

6 h
Min = 2.51×10^6
Max = 7.08×10^6

18 h
Min = 1.06×10^6
Max = 2.42×10^6

(d)

(e)
Min = 6.09×10^6
Max = 7.98×10^6

(f) White protein, AKP, BUN

(g) TBIL, TG, Glucose

(h) Heart, Liver, Spleen, Lung, Kidney

J. Fu, X. Liu, Z. Li et al.

Fig. 6. *In vivo* intelligent catalytic-therapeutic performance of MΦ–Fe$_3$O$_4$@PLGA particles against MDR *E. coli*-induced peritonitis. (a) Schematic illustration of peritonitis establishment and therapeutic outcome with the control, MΦs, Fe$_3$O$_4$@PLGA, or MΦ–Fe$_3$O$_4$@PLGA particles. (b) Blood chemistry and blood routine of each group at the time of treatment and 1 h later for n = 3 independent samples. (c) Change in CFU for different groups (control, MΦ, Fe$_3$O$_4$@PLGA, and MΦ–Fe$_3$O$_4$@PLGA groups) of major organs at 1 h. The experiment was carried out on n = 3 independent samples. (d) Concentrate of *IL-10* and *TNF-α* in ascites after treatment with control, MΦs, Fe$_3$O$_4$@PLGA, or MΦ–Fe$_3$O$_4$@PLGA particles for 1 h. The experiment was carried out on n = 3 independent samples. (e) Flow cytometric analysis of MΦs from the abdominal cavity treated with DMEM, MΦs, Fe$_3$O$_4$@PLGA, or MΦ–Fe$_3$O$_4$@PLGA particles. (f) Representative H&E staining images of heart, liver, spleen, lung, and kidney at 2 days. Inflammatory cells are marked by green arrows (scale bar = 100 μm). Data in parts (c, d) are expressed as mean ± SD. Data was analyzed by two-way ANOVA.

the liver and kidney. Furthermore, fluorescence was absent after 18 h, indicating that the MΦ–Fe$_3$O$_4$@PLGA particles were completely metabolized. The cytotoxicity of MΦ–Fe$_3$O$_4$@PLGA was then further analyzed *in vivo*. The liver and kidney function of each group were assessed to test biosafety *in vivo*. No difference was found between the groups, suggesting that MΦ–Fe$_3$O$_4$@PLGA was not toxic to the liver and kidney (Figs. 5(f) and (g)). Hematoxylin and eosin (H&E) staining of the major organs was performed to further characterize the toxicity of MΦ–Fe$_3$O$_4$@PLGA to major organs. The control and MΦ–Fe$_3$O$_4$@PLGA groups showed no obvious damage to the major organs (Fig. 5(h)). These results indicated that MΦ–Fe$_3$O$_4$@PLGA has excellent biosafety *in vivo*.

3.5. In vivo intelligent catalytic-therapeutic performance of MΦ–Fe$_3$O$_4$@PLGA particles against MDR E. coli-induced peritonitis

To further assess whether the MΦ–Fe$_3$O$_4$@PLGA particles could treat peritonitis *in vivo*, a peritonitis model was constructed by injecting MDR *E. coli* into mice (Fig. 6(a)). The control group was treated with DMEM, while the other groups were respectively treated with MΦs, Fe$_3$O$_4$@PLGA, and MΦ–Fe$_3$O$_4$@PLGA particles. After 1 h of infection, the blood of different groups was collected to perform the blood chemistry and routine analysis. White blood cells (WBCs), lymphocytes (Lymph#), monocytes (Mon#), and granulocytes (Gran#) were chosen as the evaluation index for infection. These are immune cells that participate in fighting illness and disease and thus can be used to evaluate the immune response [54,55]. As shown in Fig. 6(b), the values of WBC, Lymph#, Mon#, and Gran# in the MΦ–Fe$_3$O$_4$@PLGA group were lower than in the control, MΦs, and Fe$_3$O$_4$@PLGA groups. On the other hand, compared with the control group, the values in the MΦs and Fe$_3$O$_4$@PLGA groups were greater. These results indicated that the MΦ particles and Fe$_3$O$_4$@PLGA particles had a certain antibacterial effect *in vivo*, and that the MΦ–Fe$_3$O$_4$@PLGA particle had a strong antibacterial effect *in vivo*. The bacterial number in major organs from different groups (i.e., the control, MΦ, Fe$_3$O$_4$@PLGA, and MΦ–Fe$_3$O$_4$@PLGA groups) was characterized and is shown in Fig. 6(c). Compared with the control group, the CFU value of the MΦ, Fe$_3$O$_4$@PLGA, and MΦ–Fe$_3$O$_4$@PLGA groups was lower. Moreover, the CFU value of the MΦ–Fe$_3$O$_4$@PLGA group was even lower compared with the MΦ and Fe$_3$O$_4$@PLGA groups. These phenomena indicated that the MΦ–Fe$_3$O$_4$@PLGA particles had strong antibacterial ability and a certain protective effect on major organs *in vivo*. The bacterial value of the blood from different groups showed similar results (Fig. S13 in Appendix A). The phenotype of the MΦs in the abdominal cavity and blood was assessed via ELISA (Fig. 6(d) and Fig. S14 in Appendix A). Compared with the control group, the ratio between *IL-10* (the M2 marker) and TNF-α (the M1 marker) in the MΦ–Fe$_3$O$_4$@PLGA group was increased. This result suggested that the MΦ–Fe$_3$O$_4$@PLGA group was anti-inflammatory. FACS showed that the ratio between the M1 phenotype (CD11c$^+$CD206$^-$) and the M2 phenotype (CD11c$^-$CD206$^+$) in the control, MΦ, Fe$_3$O$_4$@PLGA, and MΦ–Fe$_3$O$_4$@PLGA groups was 8.28, 26.16, 50.13, and 55.06, respectively (Fig. 6(e)). This result was mainly due to the decreased bacterial burden in the MΦ–Fe$_3$O$_4$@PLGA group *in vivo*.

The peritoneum tissues were harvested and sectioned for immunohistochemistry staining (Fig. S15 in Appendix A). The immunohistochemistry staining of the control, MΦ, Fe$_3$O$_4$@PLGA, and MΦ–Fe$_3$O$_4$@PLGA groups showed that the expression of TNF-α in MΦ–Fe$_3$O$_4$@PLGA was down-regulated, and the expression of *IL-10* was increased (Fig. S15). Next, the H&E staining of major organs for the control, MΦ, Fe$_3$O$_4$@PLGA, and MΦ–Fe$_3$O$_4$@PLGA groups was performed at 2 day (Fig. 6(f)). In the figure, inflammatory cells are marked by green arrows in the control, MΦ, and Fe$_3$O$_4$@PLGA groups. In contrast, the MΦ–Fe$_3$O$_4$@PLGA group had

almost no inflammatory cells. These results indicated that the MΦ–Fe$_3$O$_4$@PLGA particles had a strong treatment effect on MDR *E. coli*-induced peritonitis.

4. Conclusions

In summary, this paper reported on the development of MΦ–Fe$_3$O$_4$@PLGA particles as biomimetic intelligent catalysts. The MΦ–Fe$_3$O$_4$@PLGA particles demonstrated excellent antibacterial ability through biocatalysis and Fenton catalysis. The particles were polarized into the M1 phenotype under the stimulation of MDR *E. coli*. The M1-type MΦs produced H$_2$O$_2$ and LDs through biocatalysis. Selective Fenton catalysis occurred due to the presence of H$_2$O$_2$ in the lysosome and the infectious microenvironment. LDs targeted *E. coli* and participated in the antibacterial process. More importantly, the cells' viability, integrity, and function were retained after several passages. PLGA and Fe$_3$O$_4$ NPs have been approved for use in humans by the US FDA. Overall, MΦ–Fe$_3$O$_4$@PLGA particles may become an "off-label" drug for clinical applications. Biomimetic intelligent catalysis takes full advantage of the properties of MΦs and Fe$_3$O$_4$@PLGA NPs to treat infections and can be extended to other cells and NPs to treat disease. Nevertheless, the culturing condition of living cells limits its clinical application.

Compliance with ethics guidelines

Jieni Fu, Xiangmei Liu, Zhaoyang Li, Yufeng Zheng, Yu Zhang, Hui Jiang, Yanqin Liang, Shengli Zhu, Zhenduo Cui, and Shuilin Wu declare that they have no conflict of interest or financial conflicts to disclose.

Appendix A. Supplementary data

Supplementary data to this article can be found online at https://doi.org/10.1016/j.eng.2023.05.022.

References

[1] Durand-Reville TF, Miller AA, O'Donnell JP, Wu X, Sylvester MA, Guler S, et al. Rational design of a new antibiotic class for drug-resistant infections. Nature 2021;597(7878):698–702.
[2] Lam SJ, O'Brien-Simpson NM, Pantarat N, Sulistio A, Wong EH, Chen YY, et al. Combating multidrug-resistant Gram-negative bacteria with structurally nanoengineered antimicrobial peptide polymers. Nat Microbiol 2016;1 (11):16162.
[3] Song M, Liu Y, Huang X, Ding S, Wang Y, Shen J, et al. A broad-spectrum antibiotic adjuvant reverses multidrug-resistant Gram-negative pathogens. Nat Microbiol 2020;5(8):1040–50.
[4] Bush K, Bradford PA. Interplay between β-lactamases and new β-lactamase inhibitors. Nat Rev Microbiol 2019;17(5):295–306.
[5] Walsh C. Where will new antibiotics come from? Nat Rev Microbiol 2003;1 (1):65–70.
[6] Russell CA, de Jong MD. Infectious disease management must be evolutionary. Nat Ecol Evol 2017;1(8):1053–5.
[7] Rabanal F, Cajal Y. Recent advances and perspectives in the design and development of polymyxins. Nat Prod Rep 2017;34(7):886–908.
[8] Wang Y, Zhang R, Li J, Wu Z, Yin W, Schwarz S, et al. Comprehensive resistome analysis reveals the prevalence of NDM and MCR-1 in Chinese poultry production. Nat Microbiol 2017;2(4):16260.

[9] Wang Z, Koirala B, Hernandez Y, Zimmerman M, Park S, Perlin DS, et al. A naturally inspired antibiotic to target multidrug-resistant pathogens. Nature 2022;601(7894):606–11.

[10] Ikuta KS, Sharara F, Swetschinski L, Robles Aguilar G, Gray A, Chieh H, et al. Global burden of bacterial antimicrobial resistance in 2019: a systematic analysis. Lancet 2022;399(10325):629–55.

[11] Courtney CM, Goodman SM, McDaniel JA, Madinger NE, Chatterjee A, Nagpal P. Photoexcited quantum dots for killing multidrug-resistant bacteria. Nat Mater 2016;15(5):529–34.

[12] Fu J, Liu X, Cui Z, Zheng Y, Jiang H, Zhang Y, et al. Probiotic-based nanoparticles for targeted microbiota modulation and immune restoration in bacterial pneumonia. Nat Sci Rev 2022;10(2):nwac221.

[13] Qiao Y, Xu Y, Liu X, Zheng Y, Li B, Han Y, et al. Microwave assisted antibacterial action of *Garcinia* nanoparticles on Gram-negative bacteria. Nat Commun 2022;13(1):2461.

[14] Huang X, Venet F, Wang YL, Lepape A, Yuan Z, Chen Y, et al. PD-1 expression by macrophages plays a pathologic role in altering microbial clearance and the innate inflammatory response to sepsis. Proc Natl Acad Sci U S A 2009;106 (15):6303–8.

[15] Wang P, Geng J, Gao J, Zhao H, Li J, Shi Y, et al. Macrophage achieves self-protection against oxidative stress-induced ageing through the Mst-Nrf2 axis. Nat Commun 2019;10(1):755.

[16] Fu J, Li Y, Zhang Y, Liang Y, Zheng Y, Li Z, et al. An engineered pseudo-macrophage for rapid treatment of bacteria-infected osteomyelitis *via* microwave-excited anti-infection and immunoregulation. Adv Mater 2021;33(41):2102926.

[17] Ginhoux F, Schultze JL, Murray PJ, Ochando J, Biswas SK. New insights into the multidimensional concept of macrophage ontogeny, activation and function. Nat Immunol 2016;17(1):34–40.

[18] Feuerer N, Marzi J, Brauchle EM, Carvajal Berrio DA, Billing F, Weiss M, et al. Lipidome profiling with Raman microspectroscopy identifies macrophage response to surface topographies of implant materials. Proc Natl Acad Sci U S A 2021;118(52):e2113694118.

[19] Zanganeh S, Hutter G, Spitler R, Lenkov O, Mahmoudi M, Shaw A, et al. Iron oxide nanoparticles inhibit tumour growth by inducing pro-inflammatory macrophage polarization in tumour tissues. Nat Nanotechnol 2016;11 (11):986–94.

[20] Xu J, Zheng B, Zhang S, Liao X, Tong Q, Wei G, et al. Copper sulfide nanoparticle-redirected macrophages for adoptive transfer therapy of melanoma. Adv Funct Mater 2021;31(11):2008022.

[21] Zhao X, Guo K, Zhang K, Duan S, Chen M, Zhao N, et al. Orchestrated yolk–shell nanohybrids regulate macrophage polarization and dendritic cell maturation for oncotherapy with augmented antitumor immunity. Adv Mater 2022;34 (9):2108263.

[22] Xiao Y, Fan Y, Tu W, Ning Y, Zhu M, Liu Y, et al. Multifunctional PLGA microfibrous rings enable MR imaging-guided tumor chemotherapy and metastasis inhibition through prevention of circulating tumor cell shedding. Nano Today 2021;38:101123.

[23] Chen Z, Yin JJ, Zhou YT, Zhang Y, Song L, Song M, et al. Dual enzyme-like activities of iron oxide nanoparticles and their implication for diminishing cytotoxicity. ACS Nano 2012;6(5):4001–12.

[24] Zhang CY, Gao J, Wang Z. Bioresponsive nanoparticles targeted to infectious microenvironments for sepsis management. Adv Mater 2018;30(43): e1803618.

[25] Fu J, Liu X, Tan L, Cui Z, Zheng Y, Liang Y, et al. Photoelectric-responsive extracellular matrix for bone engineering. ACS Nano 2019;13(11):13581–94.

[26] Chen X, Li L, Sun X, Liu Y, Luo B, Wang C, et al. Magnetochromatic polydiacetylene by incorporation of Fe$_3$O$_4$ nanoparticles. Angew Chem Int Ed 2011;50(24):5486–9.

[27] Chen Y, Jiang L, Wang R, Lu M, Zhang Q, Zhou Y, et al. Injectable smart phase-transformation implants for highly efficient *in vivo* magnetic-hyperthermia regression of tumors. Adv Mater 2014;26(44):7468–73.

[28] Zheng J, Liu ZQ, Zhao XS, Liu M, Liu X, Chu W. One-step solvothermal synthesis of Fe$_3$O$_4$@C core–shell nanoparticles with tunable sizes. Nanotechnology 2012;23(16):165601.

[29] Wilhelm C, Gazeau F, Roger J, Pons JN, Bacri JC. Interaction of anionic superparamagnetic nanoparticles with cells: kinetic analyses of membrane adsorption and subsequent internalization. Langmuir 2002;18(21):8148–55.

[30] Verma NK, Crosbie-Staunton K, Satti A, Gallagher S, Ryan KB, Doody T, et al. Magnetic core–shell nanoparticles for drug delivery by nebulization. J Nanobiotechnology 2013;11(1):1–12.

[31] Tansık G, Yakar A, Gündüz U. Tailoring magnetic PLGA nanoparticles suitable for doxorubicin delivery. J Nanopart Res 2013;16(1):1–13.

[32] Hurbankova M, Volkovova K, Hraskova D, Wimmerova S, Moricova S. Respiratory toxicity of Fe$_3$O$_4$ nanoparticles: experimental study. Rev Environ Health 2017;32(1–2):207–10.

[33] Zhang X, Zhang H, Liang X, Zhang J, Tao W, Zhu X, et al. Iron oxide nanoparticles induce autophagosome accumulation through multiple mechanisms: lysosome impairment, mitochondrial damage, and ER stress. Mol Pharm 2016;13(7):2578–87.

[34] Yao J, Wu D, Zhang C, Yan T, Zhao Y, Shen H, et al. Macrophage IRX3 promotes diet-induced obesity and metabolic inflammation. Nat Immunol 2021;22 (10):1268–79.

[35] Schoelmerich MC, Katsyv A, Dönig J, Hackmann TJ, Müller V. Energy conservation involving 2 respiratory circuits. Proc Natl Acad Sci U S A 2020;117(2):1167–73.

[36] Yang L, Xie M, Yang M, Yu Y, Zhu S, Hou W, et al. PKM2 regulates the Warburg effect and promotes HMGB1 release in sepsis. Nat Commun 2014;5(1):4436.

[37] Russell DG, Huang L, VanderVen BC. Immunometabolism at the interface between macrophages and pathogens. Nat Rev Immunol 2019;19(5):291–304.

[38] Tan L, Fu J, Feng F, Liu X, Cui Z, Li B, et al. Engineered probiotics biofilm enhances osseointegration via immunoregulation and anti-infection. Sci Adv 2020;6(46):eaba5723.

[39] Zhu Y, Liang H, Liu X, Wu J, Yang C, Wong TM, et al. Regulation of macrophage polarization through surface topography design to facilitate implant-to-bone osseointegration. Sci Adv 2021;7(14):eabf6654.

[40] Sindrilaru A, Peters T, Wieschalka S, Baican C, Baican A, Peter H, et al. An unrestrained proinflammatory M1 macrophage population induced by iron impairs wound healing in humans and mice. J Clin Invest 2011;121(3):985–97.

[41] Bosch M, Sánchez-Álvarez M, Fajardo A, Kapetanovic R, Steiner B, Dutra F, et al. Mammalian lipid droplets are innate immune hubs integrating cell metabolism and host defense. Science 2020;370(6514):eaay8085.

[42] Kim JK, Uchiyama S, Gong H, Stream A, Zhang L, Nizet V. Engineered biomimetic platelet membrane-coated nanoparticles block *Staphylococcus aureus* cytotoxicity and protect against lethal systemic infection. Engineering 2021;7(8):1149–56.

[43] Wu J, Yu Y, Cheng Y, Cheng C, Zhang Y, Jiang B, et al. Ligand-dependent activity engineering of glutathione peroxidase-mimicking MIL-47(V) metal–organic framework nanozyme for therapy. Angew Chem Int Ed 2021;60(3):1227–34.

[44] Duan X, Li Y. Physicochemical characteristics of nanoparticles affect circulation, biodistribution, cellular internalization, and trafficking. Small 2013;9(9–10):1521–32.

[45] Chu PS, Nakamoto N, Ebinuma H, Usui S, Saeki K, Matsumoto A, et al. C-C motif chemokine receptor 9 positive macrophages activate hepatic stellate cells and promote liver fibrosis in mice. Hepatology 2013;58(1):337–50.

[46] Arabpour M, Saghazadeh A, Rezaei N. Anti-inflammatory and M2 macrophage polarization-promoting effect of mesenchymal stem cell-derived exosomes. Int Immunopharmacol 2021;97:107823.

[47] Cui J, Wu X, Song Y, Chen Y, Wan J. Complement C3 exacerbates renal interstitial fibrosis by facilitating the M1 macrophage phenotype in a mouse model of unilateral ureteral obstruction. Am J Physiol Renal Physiol 2019;317 (5):F1171–82.

[48] Van Zuijlen WJM, Schroder K, Garceau V, Sweet MJ, Kellie S, Hume DA. Expression and function of Schlafen-4 in macrophage biology and inflammation. Cytokine 2008;43(3):246.

[49] Signorelli P, Pivari F, Barcella M, Merelli I, Zulueta A, Dei Cas M, et al. Myriocin modulates the altered lipid metabolism and storage in cystic fibrosis. Cell Signal 2021;81:109928.

[50] Wathes DC, Cheng Z, Salavati M, Buggiotti L, Takeda H, Tang L, et al. Relationships between metabolic profiles and gene expression in liver and leukocytes of dairy cows in early lactation. J Dairy Sci 2021;104(3):3596–616.

[51] Huang F, Liao F, Ma G, Hu Y, Zhang C, Xu P, et al. TBRG4 knockdown suppresses proliferation and growth of human osteosarcoma cell lines MG63 through PI3K/Akt pathway. OncoTargets Ther 2020;13:7271–81.

[52] Thorek DLJ, Chen AK, Czupryna J, Tsourkas A. Superparamagnetic iron oxide nanoparticle probes for molecular imaging. Ann Biomed Eng 2006;34 (1):23–38.

[53] Zhang C, Bu W, Ni D, Zhang S, Li Q, Yao Z, et al. Synthesis of iron nanometallic glasses and their application in cancer therapy by a localized Fenton reaction. Angew Chem Int Ed Engl 2016;55(6):2101–6.

[54] Liu H, Li J, Liu X, Li Z, Zhang Y, Liang Y, et al. Photo–sono interfacial engineering exciting the intrinsic property of herbal nanomedicine for rapid broad-spectrum bacteria killing. ACS Nano 2021;15(11):18505–19.

[55] Jin L, Liu X, Zheng Y, Li Z, Zhang Y, Zhu S, et al. Interface polarization strengthened microwave catalysis of MoS$_2$/FeS/Rhein for the therapy of bacteria-infected osteomyelitis. Adv Funct Mater 2022;32(33):2204437.